Near- and sub-barrier fusion of ^{20}O incident ions with ^{12}C target nuclei

M. J. Rudolph, Z. Q. Gosser, K. Brown, S. Hudan, and R. T. de Souza[*]

Department of Chemistry and Center for Exploration of Energy and Matter 2401 Milo B. Sampson Lane,
Bloomington, Indiana 47405, USA

A. Chbihi and B. Jacquot

GANIL, Caen, France

M. Famiano

Department of Physics, Western Michigan University, Kalamazoo, Michigan, USA

J. F. Liang and D. Shapira

Oak Ridge National Laboratory, Physics Division, Oak Ridge, Tennessee 37831, USA

D. Mercier

Centre de Calcul du CNRS/IN2P3, Domaine Scientifique de La Doua, Villeurbanne, France

Evaporation residues resulting from fusion of ^{20}O incident ions with ^{12}C target nuclei have been measured for the first time. The cross-section associated with compound nuclei that de-excite via emission of charged particles is extracted. The resulting excitation function is compared with the predictions of a standard fusion model followed by statistical decay code. A significant underprediction of the measured cross-section by the fusion-evaporation model raises the question of whether the fusion cross-section is larger for the neutron-rich projectile or the statistical de-excitation is incorrectly predicted.

I. INTRODUCTION

Neutron stars are fascinating objects providing a broad range of nuclear density from sub-saturation to super-saturation at relatively low temperature [1]. The outer crust of an accreting neutron star is particularly interesting as it presents a unique environment for nuclear reactions to occur. At the density of the outer crust, the electron Fermi level becomes sufficiently large to lead to electron capture reactions, resulting in neutron-rich nuclei [2]. Isotopes of nuclei ranging from oxygen to iron have been calculated to be produced in this environment. It has been proposed that these nuclei, though present at the level of contaminants [3,4], may play an important role in the behavior of the neutron star. For example, it has been proposed that enhanced fusion between light neutron-rich nuclei below the Coulomb barrier might provide an additional heat source necessary to ignite the carbon burning intimated to be responsible for the phenomenon of x-ray superbursts [5]. Radioactive beam facilities provide the opportunity to explore these possibilities experimentally.

In order to investigate whether fusion between neutron-rich light nuclei is enhanced as compared to fusion of β-stable nuclei, it is necessary to develop an appropriate experimental technique. While fusion studies with neutron-rich heavy beams such as ^{132}Sn on Ni targets have been conducted, these experiments utilize inverse kinematics [6]. For such inverse kinematics bombardments the importance of detection thresholds is

reduced and the laboratory angular distribution of the reaction products is narrowed, aiding the measurement of the fusion products. As the reactions estimated to be a potential heat source in the neutron star crust involve symmetric collisions such as ^{24}O + ^{24}O [2], one cannot benefit from kinematic focusing as in the ^{132}Sn induced reactions. Based upon the intensities of the neutron-rich oxygen isotopes available we elected to measure the fusion cross-section in the reaction ^{20}O + ^{12}C. Our goal in the present work was twofold. In addition to developing an experimental technique suitable for measuring fusion induced by neutron-rich light ions in symmetric systems near and below the Coulomb barrier, we also aimed to measure the total fusion cross-section for the system ^{20}O + ^{12}C.

II. EXPERIMENTAL SETUP

The experiment was conducted at the GANIL-SPIRAL facility in Caen, France by bombarding a natural ^{12}C target with a radioactive beam of ^{20}O ions. A primary beam of ^{22}Ne accelerated to an energy of 79 MeV/nucleon impinged on a carbon production target. From this primary target, a ^{20}O beam was extracted, reaccelerated by the CIME cyclotron to an energy of 3 MeV/nucleon, and transported to the experimental area. This incident energy was the minimum energy that could be delivered by the beam transport system. The beam intensity at the target was typically $\approx$1–2 $\times$ 10^4 p/s. Depicted in Fig. 1 is the experimental setup used in the measurement. The detectors used in the experiment were situated in a rectangular stainless steel scattering chamber that was evacuated to a pressure of $\approx$2 $\times$ 10^{-6} torr. This chamber
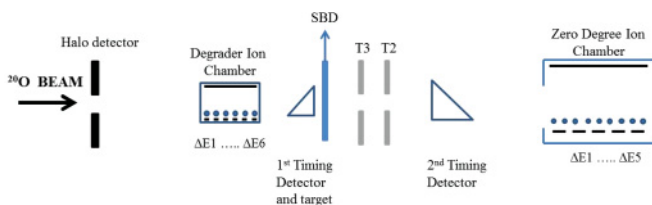
*desouza@indiana.edu

FIG. 1. (Color online) Experimental setup used to measure the fusion of incident ^{20}O ions with ^{12}C target nuclei.

measured approximately 105 cm × 35.6 cm × 29.7 cm with the long axis situated along the beam direction. At the entrance of the chamber was an annular fast-plastic detector readout by a photomultiplier tube. This detector which had a 13 mm diameter hole was used to reject beam halo. Just upstream of the target was a retractable, multianode ionization chamber (CID). This standard, transverse-field Frisch-gridded ion chamber served two purposes. Its principal purpose was to degrade the initial beam energy from $E/A = 3$ MeV to the desired range of $E/A = 1$–2 MeV. This attenuation was accomplished by passing the ^{20}O ions through CID operated at a pressure of $P = 89.5$–180.1 mbar of CF_4. Tests conducted prior to the experiment at HRIBF-ORNL demonstrated that the divergence incurred by this degrading of the beam from $E/A = 3$ MeV to 1 MeV was tolerable. As determining the purity of the beam is a critical issue in radioactive beam experiments, CID also provided a continuous measurement of the beam identity and purity. Shown in the left panel of Fig. 2 is the energy spectrum measured during the experiment on one of the CID anodes. The dominant peak visible is due to the incident ^{20}O beam. At slightly higher energy than the dominant peak is a peak attributed to the principal contaminant expected in the radioactive beam, namely ^{20}F. This peak assignment was checked at the end of the experiment by tuning the CIME cyclotron to accelerate ^{20}F rather than ^{20}O. The resulting CID anode energy spectrum is displayed in the right panel of

Fig. 2. The peak assigned to ^{20}F becomes dominant as expected confirming the peak assignment. Throughout the experiment ^{20}O ions were selected on an event-by-event basis by utilizing their energy loss measured in CID. Directly after CID on a retractable mount was a silicon surface barrier detector. Periodically during the experiment, the beam intensity was decreased and the surface barrier detector was inserted in order to measure both the average energy and energy dispersion of the beam after degrading.

Immediately downstream of CID was a microchannel plate detector that served as a compact time-zero detector [7]. The 100 μg/cm^2 carbon foil in this detector served as both an electron emission foil as well as the target for the experiment. Electrons ejected from this foil, due to the passage of ^{20}O ions through it, were accelerated by a wire harp and then reflected by an electrostatic mirror onto the surface of a chevron microchannel plate (MCP) stack. Amplification of the primary electrons by the MCP provided a fast time signal for the subsequent time-of-flight measurement.

In the near Coulomb barrier energy domain investigated, compound nuclei produced by fusion reactions de-excite by emission of neutrons, protons, and α particles, deflecting the resulting evaporation residue from zero degrees. Consequently, a large fraction of the residue cross-section is calculated to be observed in the angular range $3° \leqslant \theta_{lab} \leqslant 20°$ [8,9]. Evaporation residues and light charged particles emitted in the reaction were detected by two annular silicon detectors situated 12 cm (T3) and 17.8 cm (T2) downstream of the target which subtended the angular range $11.3° \leqslant \theta_{lab} \leqslant 21.8°$ and $3.5° \leqslant \theta_{lab} \leqslant 10.8°$, respectively. This angular coverage results in the detectors subtending a solid angle of 327 msr and 99 msr in the laboratory, respectively. These annular silicons are highly segmented ion-implanted passivated detectors [10] with pie-shaped sectors on their ohmic surface and rings on their junction side. Signals from the pie sectors were used to provide both fast timing signals, as well as energy signals while signals from the rings provided additional energy information. Signals from both rings and pies determined the angular emission direction of the charged particle. The sub-nanosecond timing achieved with such segmented detectors has been previously described [11].

Evaporation residues produced in the angular range $\theta_{lab} \leqslant 3.5°$ were detected by a 40 mm diameter MCP located along the beam axis followed by a zero degree ionization chamber (ZDIC). This ZDIC detector employed the same transverse field, Frisch-grid design as CID but had fifteen anodes arranged in a 5×3 geometry with five anodes oriented along the beam direction. It was operated with a fill gas of CF_4 at a pressure of $P = 20$–47 mbar. Beam running continuously through ZDIC required the center anodes to separate evaporation residues from a constant beam background of 10^4 p/s, however the segmentation transverse to the beam resulted in a smaller beam background at larger angles $1.0° \leqslant \theta_{lab} \leqslant 3.0°$.
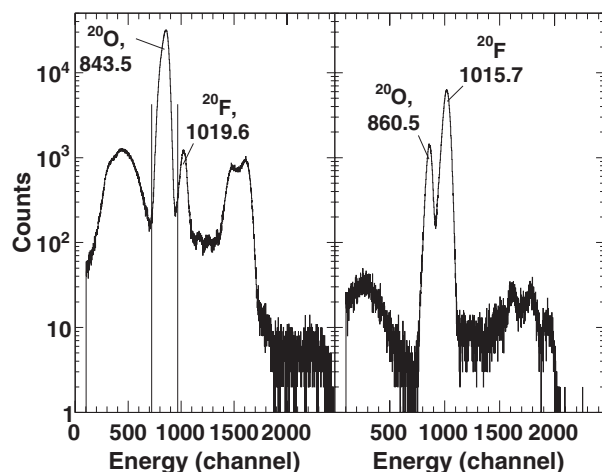

FIG. 2. Left panel: Energy spectra from one of the anodes of the degrader ionization chamber CID with the incident ^{20}O beam. Right panel: Energy spectra from the same CID anode when the CIME cyclotron was tuned to ^{20}F at the end of the experiment.

III. EXPERIMENTAL RESULTS

Displayed in Fig. 3 is a two-dimensional spectrum of the energy versus time-of-flight for particles entering the T2
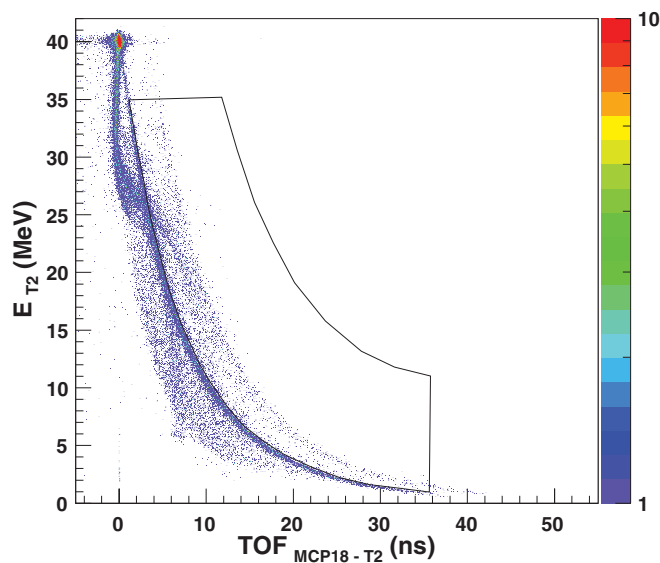
FIG. 3. (Color online) Two-dimensional energy-TOF spectrum for particles detected in the T2 detector. The polygonal gate indicates the region used to search for coincidences between evaporation residues in T2 and light charged particles in T3. See text for details.

FIG. 4. (Color online) Two-dimensional energy-TOF spectrum for particles detected in the T3 detector.

detector. The energy displayed is the energy deposited in the silicon detector while the time-of-flight corresponds to the time-of-flight between the target MCP (designated MCP18) and the T2 detector. Clearly evident is the prominent elastic peak with an energy of $\approx$40 MeV. Originating from the elastic peak and extending down to approximately 25 MeV is a near vertical band. Particles along this locus have a time-of-flight consistent with elastically scattered particles. For these particles, a lower energy is measured due to the incomplete collection of charge by the silicon detector. Walk of the leading edge discriminators used for the silicon timing signals is responsible for the slight positive slope of this band. This incomplete charge collection occurs despite the detector being biased to -80 V, well above the manufacturer's nominal full depletion value. Biasing at a voltage of -90 V did not noticeably reduce the incomplete charge collection problem. A quoted breakdown voltage of -100 V prevented biasing the detector to a substantially higher value during the experiment. Also evident in the spectrum is a locus of points originating from the elastic peak and increasing in time as the deposited energy decreases. Points along this locus correspond to particles degraded in energy prior to entering the silicon detector. Consequently, their measured time-of-flight reflects their degraded energy. Slit scattering of particles from the acceleration and reflecting grids of the target MCP detector is the most likely source of the energy loss. Located below the slit scatter line is a haze corresponding to slit scattered particles for which incomplete charge collection occurs. Located at higher energies and longer times with respect to the slit scatter line is yet another locus of points. This locus exhibits a similar energy-time relationship as the slit scatter line. The large cross-section of $\approx$50–70 barns associated with these points clearly indicates that they have an atomic and not nuclear origin. However, as they occupy the same region of the energy-TOF spectrum as that expected by the evaporation residues they
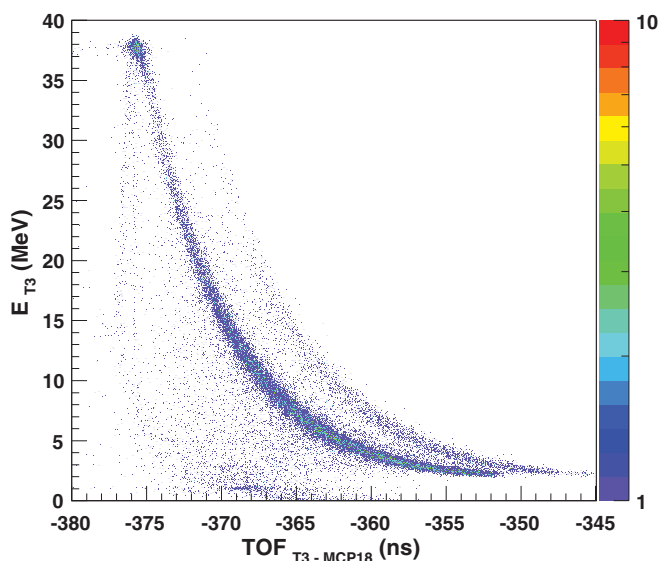
represent a daunting background for measuring the fusion cross-section. Subsequent to the experiment, bench tests with alpha sources conclusively demonstrated that scattering from the reflecting grids of the MCP provided a false early start signal resulting in this background.

The energy-TOF spectrum for particles entering the T3 detector is displayed in Fig. 4. While the principal spectral features of the elastic peak, incomplete charge collection, and slit scatter line observed for T2 also exist for T3, it is interesting to note that the incomplete charge collection in T3 appears to be significantly less severe than for T2. The background due to false early target MCP signals from the reflecting grid is also evident in this detector supporting the result that the problem arises from the MCP detector and not the T2 silicon detector.

The presence of the large atomic background in the experiment due to scattering from the wire grids in the beam path precludes extraction of the total fusion cross-section. It clearly indicates that to successfully measure the total fusion cross-section in the future requires eliminating all such grids. Having failed to measure the desired total fusion cross-sections, to extract some useful information from the present data set, we explored whether the fusion process could be separated from the atomic background by requiring a coincidence. Evaporation residues produced in the experiment result from de-excitation following the fusion reaction. While for the neutron-rich compound nucleus one expects neutron emission to be the principal means of de-excitation, it is also possible that charged particle channels are involved. Emission of charged particles could in principle provide a tag by which to separate fusion events from the slit scattering background. The nuclide composition of the evaporation residue distribution can be calculated by utilizing a multiparticle Monte Carlo evaporation code such as EVAPOR [12]. This model uses a simple fusion model (Bass) [13] to predict the fusion cross-section, followed by a Hauser-Feschbach approach to model its subsequent decay.

TABLE I. Predictions of the EVAPOR model of the percentage of the evaporation residue distribution populated by various nuclides.

Nuclide	22 MeV	27 MeV	42 MeV
^{30}Si	40.5	31.8	15.9
^{29}Si	43.6	51.2	56.9
^{30}Al	5.3	4.0	2.3
^{29}Al	1.4	2.5	5.4
^{27}Mg	7.5	8.4	8.3
^{26}Mg		1.5	9.0

Calculations were performed at incident energies varying from $E_{lab} = 20$ MeV to $E_{lab} = 45$ MeV assuming a triangular angular momentum distribution. In Table I, the percentage of the evaporation distribution attributable to various nuclides is shown for three incident energies. Even at the lowest energy, $E_{lab} = 22$ MeV, while 84% of the residues are formed through purely neutron decay channels, a significant fraction of the evaporation residue yield, $\approx 16\%$, is formed through some charged particle emission. With increasing incident energy, the percentage of yield involving some charged particle emission increases to 27% at $E = 42$ MeV. Similar results are obtained with the statistical decay code PACE [9].

To extract fusion events from the large atomic background evident in Figs. 3 and 4, we required a coincidence between detection of an evaporation residue in $T2$ and a charged particle in $T3$. The potential region of interest for evaporation residues is well-defined by the slit-scatter line in Fig. 3 and extends to longer times. It is indicated by the polygonal gate displayed in Fig. 3. Coincident with detection of a particle in this gate a particle in $T3$ was required. All coincident particles in $T3$ are clustered in time with a time spread of ≈ 2 ns. This time spread of the charged particle in $T3$, short compared to the RF beam burst period of 100 ns, indicates that random coincidences play no significant role. This result is hardly surprising due to the low beam intensity. The E-TOF spectra of coincidences in $T2$ is shown in Fig. 5 for three incident energies. For reference the position of the slit scatter line is indicated as a solid line. It should be noted that the energy depicted corresponds to the energy measured in the silicon detector. At the highest incident energy, $E_{lab} = 41.0$ MeV, all of the coincident particles are clustered in the range 8 MeV$\leqslant E \leqslant 22$ MeV. At the intermediate energy, $E_{lab} = 25.0$ MeV, although particles for the most part are clustered in the same energy range, a couple of particles are observed with $E \leqslant 5$ MeV. At the lowest incident energy, $E_{lab} = 19.8$ MeV, the detected energies are significantly lower, $E \leqslant 13$ MeV.

To ascertain whether the measured energies for evaporation residues and light charged particles match the expected energies for these reaction products, we compared the experimental data with the predictions of the statistical model code EVAPOR [12]. Evaporation residues and light charged particles from the model were subsequently filtered by the geometrical acceptance of the experimental setup and detection thresholds were accounted for. The efficiency for detecting a light charged particle (LCP) in coincidence with a residue in $T2$ is principally determined by the small solid angle of the $T3$ detector and the isotropic emission of the LCPs. As evident
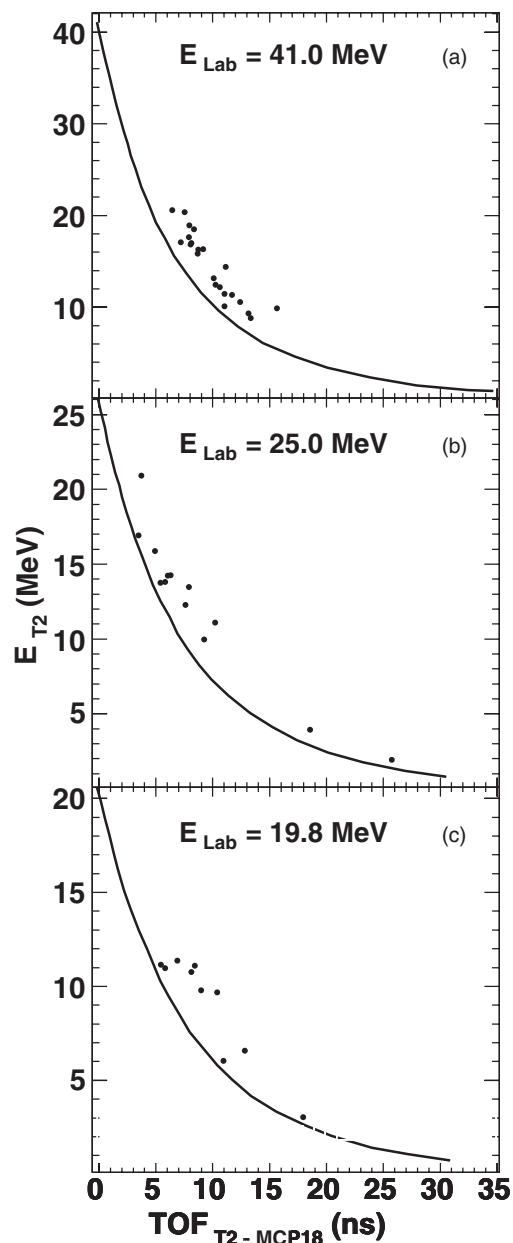

FIG. 5. Energy-TOF spectra of particles in the $T2$ detector observed in coincidence with a charged particle in $T3$. The solid line indicates the position of the slit-scatter line observed in Fig. 3.

in Fig. 6 this efficiency is relatively constant with incident energy and approximately 3.0% to 3.5%. The efficiency calculations include the influence of the finite beam spot size as well as multiple scattering in CID. The beam spot size was assumed to be a gaussian with a width of 7 mm at 4σ, based upon beam optics calculations. The multiple scattering in CID as a function of pressure was determined by an experimental measurement at OakRidge National Laboratory. In this experiment, a low-intensity beam of 3 MeV/nucleon ^{18}O was passed through a gas cell containing CF_4 and the resulting beam spot was imaged on a multiwire proportional counter located downstream. It is evident from Fig. 6 that neither the multiple scattering in CID nor the finite beam
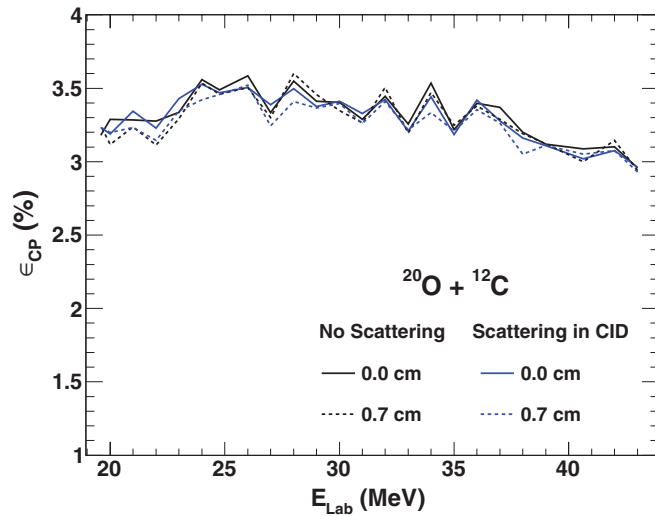
FIG. 6. (Color online) Efficiency for detecting the residue and light charged particle.

spot has a significant influence on the calculated coincidence efficiency.

Presented in Fig. 7 are the energy distributions for evaporation residues (left column) and LCPs (right column) measured in the experiment (solid line), together with the predictions of the EVAPOR model (dashed red line). As we do not experimentally determine the identity of the light charged particle, the predicted energy distributions shown are summed over all charged particles. The predicted distributions for both evaporation residues, as well as light charged particles, have been corrected for energy loss in half the target as well as a nominal dead layer on the surface of the silicon detectors. The thickness of this dead layer was assumed to have an effective thickness of 0.7 μm Si equivalent, consistent with similar detectors [14]. The model predictions have been arbitrarily scaled for clarity, as indicated in the figure. It is evident that at all three incident energies shown, the energy distributions for the evaporation residues are in reasonable agreement with the model calculations though at the highest incident energy the experimental energies are lower by approximately 5.5 MeV. In the case of the light charged particle spectra, somewhat larger differences between the measured and predicted distributions are observed. Some of the difference between the measured and predicted distributions may arise because of differences between the emitted particles produced and those predicted.

Having corrected for the geometric efficiency, it is possible to extract the cross-section associated with fusion followed by charged particle emission, σ_{CP}. The total number of incident beam particles was determined from the target MCP detector and crosschecked against the CID detector at the running intensity and the SBD detector at low intensity. In both cases, the integrated counts of the target MCP and the other two detectors were in reasonable agreement though the integrated counts in CID were typically 10% higher. This slightly larger number of counts in CID can be understood due to the divergence of the beam on degrading. The resulting cross-sections are presented in Fig. 8. These measured cross-sections decrease with decreasing incident energy from 492 $\pm$ 105 mb
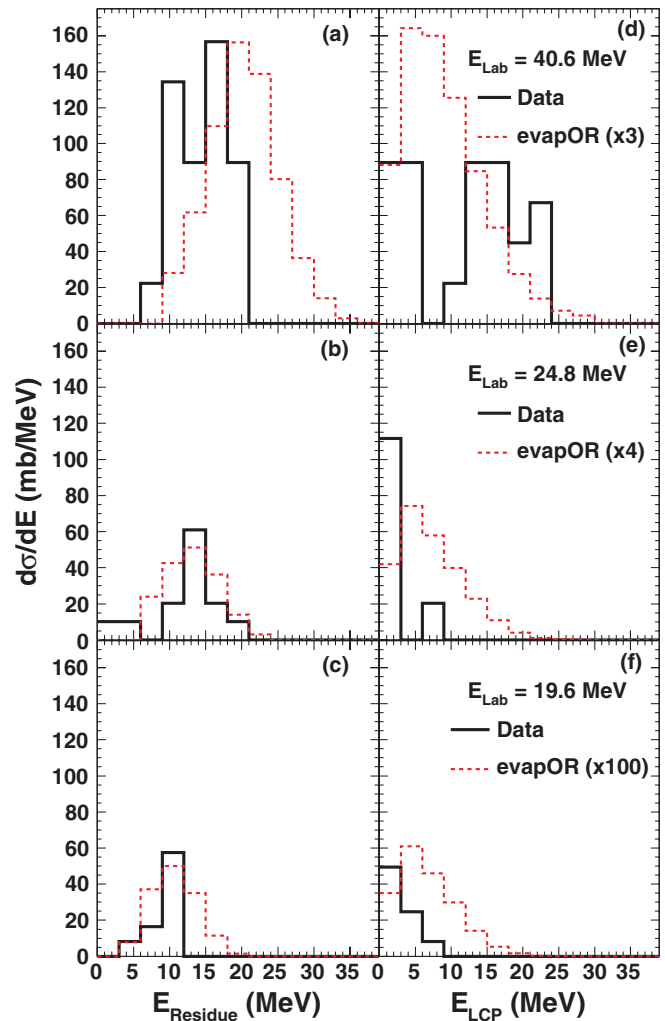

FIG. 7. (Color online) Energy distribution of light charged particles and residues compared to predictions of the statistical model EVAPOR.

at $E_{lab} = 40.6 \pm 0.286$ MeV to 82.3 mb $\pm$ 26 at $E_{lab} = 19.6 \pm 0.449$ MeV. Vertical error bars reflect the statistical errors associated with the measurement while horizontal error bars indicate the dispersion (σ) in incident energy due to degrading the incident beam and the energy dispersion due to the target.

The observed change in the cross-section with energy is influenced by both the overall decrease in the fusion cross-section with decreasing energy, as well as changes in the population of charged particle decay channels with decreasing energy. Shown for comparison in Fig. 8 are the predictions for both the total fusion cross-section (solid line) and the cross-section associated with charged particle channels (dashed line) predicted by the EVAPOR model. Comparison of the experimental data with the model predictions yields two significant results. The first noteworthy point is that the measured cross-sections exceed those predicted by the model for the charged particle channels by a factor of $\approx$2. This is true at all incident energies including the highest incident energy which is well above the Coulomb barrier. The second interesting result is that the dependence of the experimental
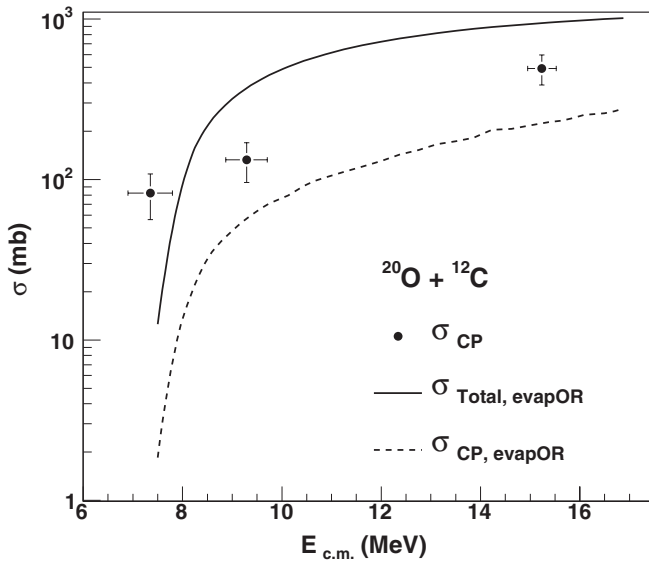
FIG. 8. Measured fusion cross-sections associated with charged particle emission channels (solid points) compared to the predictions of the evapOR model. The total predicted fusion cross-section is shown as a solid line while the cross-section predicted for the charged particle channels is represented by the dashed line. Horizontal error bars on the data points reflect the energy dispersion due to degrading the incident beam.

cross-section with decreasing incident energy is weaker than that predicted by the fusion-evaporation model. Each of these observations is independently interesting. For example, if one might question the uncertainty involved with degrading the incident beam to the lowest incident energy, the impact of this uncertainty in energy is significantly less, and less important for the highest energy point where the excitation function is relatively flat. Thus, the larger cross-section at the highest energy point is particularly noteworthy.

In critically examining the measured cross-section for the charged particle channels following fusion one needs to examine the role of the statistical model in extracting the cross-section. In order to deduce a cross-section it is essential to understand the efficiency of the experimental setup. While the geometry of the experimental setup is well defined, determining the efficiency in turn relies on the statistical model correctly predicting the decay channels, as well as the energy and angular distributions of the emitted charged particles and evaporation residue. The larger measured cross-section as compared to the EVAPOR model could reflect a failure on the part of the statistical model to correctly describe the de-excitation of the neutron-rich compound nucleus. This discrepancy suggests that in addition to measuring the total fusion cross-section future work to examine the de-excitation of neutron-rich light nuclei may be valuable.

IV. FUSION IN ^{16}O + ^{12}C

To provide a reference for the fusion of neutron-rich oxygen and carbon nuclei as well as ascertain whether the simple fusion model correctly predicts the fusion cross-section for
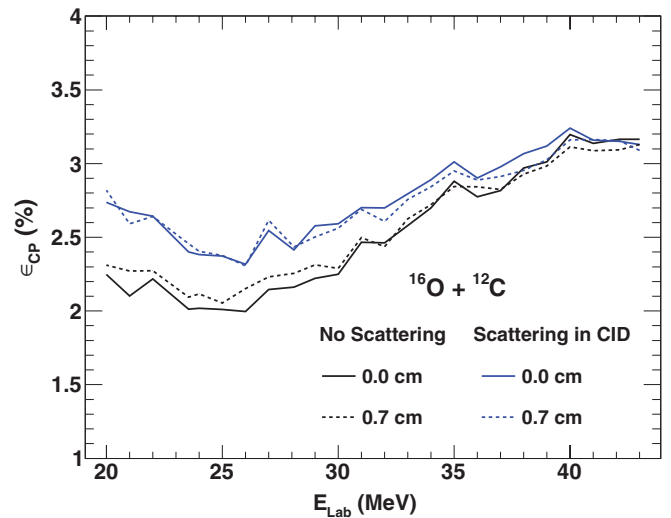

FIG. 9. (Color online) Efficiency for detecting the residue and light charged particle in the reaction ^{16}O + ^{12}C measured at GANIL.

β-stable nuclei, we measured the reaction ^{16}O + ^{12}C immediately following the ^{20}O beamtime with the identical setup. The subsequent analysis of the experimental data closely followed the analysis performed for the ^{20}O induced reaction. The efficiency for detecting light charged particles in coincidence with fusion residues is shown in Fig. 9. In contrast to the efficiency calculations for the ^{20}O reaction shown in Fig. 6, a dependence on the multiple scattering in CID is observed as well as an overall general increase with incident energy. With
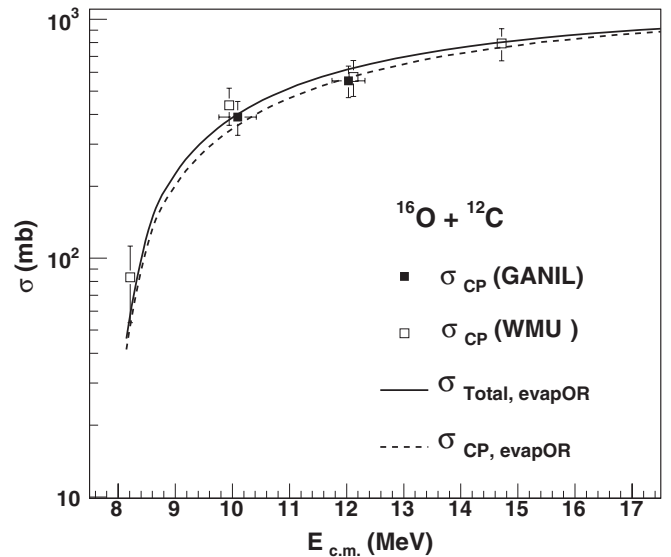

FIG. 10. Measured fusion cross-sections from the reaction ^{16}O + ^{12}C associated with charged particle emission channels (solid points) compared to the predictions of the EVAPOR model. The total predicted fusion cross-section is shown as a solid line while the cross-section predicted for the charged particle channels is represented by the dashed line. Horizontal error bars on the data points measured at GANIL reflect the energy dispersion due to degrading the incident beam.

TABLE II. Predictions of the EVAPOR model of the percentage of the evaporation residue distribution for different nuclides in the reaction ^{16}O $+$ ^{12}C.

Nuclide	24 MeV	35 MeV
^{27}Si	10.8	4.7
^{27}Al	63.9	29.2
^{26}Al	2.0	17.6
^{26}Mg	6.0	24.7
^{24}Mg	16.4	15.3
^{23}Na	0.3	3.4
^{20}Ne	0.5	5.1

increasing incident energy, namely decreasing pressure in CID, the influence of the multiple scattering in CID diminishes as expected.

Shown in Fig. 10 as the solid points is the extracted fusion cross-section that decays by charged particle emission. In contrast to the decay of ^{32}Si*, the fusion product of this reaction, ^{28}Si*, decays principally by charged particle emission as indicated in Table II. For comparison with the experimental data the total fusion cross-section as well as the fusion cross-section associated with charged particle decay predicted by EVAPOR are shown as the solid and dashed lines, respectively. It is apparent that the measured cross-section agrees well with the model prediction. This agreement indicates that the model does a good job of predicting the fusion cross-section of the reaction ^{16}O $+$ ^{12}C and the subsequent charged particle de-excitation of the ^{28}Si*.

Due to the fact that only two data points exist from our ^{16}O measurement, we subsequently performed an experiment at Western Michigan University. A beam of ^{16}O was accelerated by the 6 MV tandem to energies between 20 and 35 MeV and impinged on a 100 μg/cm^2 carbon foil. This target foil also served as the electron emission foil of the target MCP. As the beam energy could be easily varied and a low energy beam could be transported, there was no need to degrade the beam energy as was done in the prior experiment. Consequently, the uncertainty in the energy is determined by the tandem accelerator and is typically of the order of $\leqslant$20 keV. Evaporation residues and light charged particles were detected with silicon detectors as in the GANIL experiment. Evaporation residues, in T2, coincident with light charged particles in $T3$ were identified by their energy and time-of-flight. The resulting

data are shown in Fig. 10 as the open symbols. The agreement of this data with the predicted excitation function bolsters our confidence in the ^{20}O results.

V. CONCLUSIONS

This first attempt to measure the total fusion cross-section in the system ^{20}O and ^{12}C demonstrated that while the overall approach utilized appears feasible, there are still some technical obstacles to overcome. Most notably it is necessary to eliminate slit scattering if one is to measure the fusion excitation function. As the largest source of slit scattering is from the MCP acceleration and electrostatic reflection grids, we are presently developing a gridless MCP design to circumvent this problem. Despite this setback with the present data set, we have successfully extracted the cross-section for a fraction of the fusion cross-section, namely the case in which fusion is followed by emission of at least one charged particle. For these channels, the measured cross-section exceeds that of a simple fusion model. In comparison, for the fusion of β stable ^{16}O with ^{12}C this fusion-evaporation model correctly predicts the measured cross-section for the charged particle decay channels. This underprediction of the cross-section by the model for the neutron-rich projectile could point to either an overall enhancement of the fusion cross-section, or may indicate that the competition between charged particle emission and neutron decay in the de-excitation phase is incorrectly extrapolated by the statistical model from the ^{16}O and ^{12}C system. The present data suggests that future experiments to measure the total fusion cross-section should also attempt to measure both the neutron and charged particle de-excitation channels. Such data might provide new insights on the fusion of neutron-rich light nuclei and their subsequent de-excitation, stimulating comparison with more sophisticated fusion models.

[1] J. M. Lattimer and M. Prakash, Science **304**, 536 (2004).
[2] C. J. Horowitz, H. Dussan, and D. K. Berry, Phys. Rev. C **77**, 045807 (2008).
[3] C. J. Horowitz, O. L. Caballero, D. K. Berry, Phys. Rev. E **79**, 026103 (2009).
[4] C. J. Horowitz, D. K. Berry, Phys. Rev. C **79**, 065803 (2009).
[5] T. Strohmayer and L. Bildsten, *Compact X-ray Stellar Sources* (Cambridge University, Cambridge, 2006).
[6] D. Shapira, J. F. Liang, C. J. Gross, R. L. Varner, H. Amro, C. Harlin, J. J. Kolata, and S. Novotny, Nucl. Instrum. Methods Phys. Res. A **551**, 330 (2005).
[7] W. Starzecki, A. M. Stefanini, S. Lunardi, and C. Signorini, Nucl. Instrum. Methods Phys. Res. **193**, 499 (1982).
[8] O. B. Tarasov and D. Bazin, Phys. At. Nucl. **66**, 1578 (2003).
[9] A. Gavron, Phys. Rev. C **21**, 230 (1980).
[10] MicronSemiconductor [www.micronsemiconductor.co.uk].

[11] R. T. deSouza, A. Alexander, K. Brown, B. Floyd, Z. Q. Gosser, S. Hudan, J. Poehlman, and M. J. Rudolph, Nucl. Instrum. Methods Phys. Res. A **632**, 133 (2011).

[12] N. G. Nicolis and J. R.Beene (1993) (unpublished).

[13] R. Bass, Phys. Rev. Lett. **39**, 265 (1977).

[14] D. Fox, R. T. de Souza, S. L. Chen, B. Davin, T. M. Hamilton, Y. Lou, J. Dorsett, and J. Ottarson, Nucl. Instrum. Methods Phys. Res. A **368**, 709 (1996).